

# Hadean isotopic fractionation of xenon retained in deep silicates

<https://doi.org/10.1038/s41586-022-04710-4>

Igor Rzeplinski<sup>1</sup>, Chrystèle Sanloup<sup>1✉</sup>, Eric Gilibert<sup>2</sup> & Denis Horlait<sup>2</sup>

Received: 30 April 2021

Accepted: 31 March 2022

Published online: 22 June 2022

 Check for updates

Our understanding of atmosphere formation essentially relies on noble gases and their isotopes, with xenon (Xe) being a key tracer of the early planetary stages. A long-standing issue, however, is the origin of atmospheric depletion in Xe<sup>1</sup> and its light isotopes for the Earth<sup>2</sup> and Mars<sup>3</sup>. Here we report that feldspar and olivine samples confined at high pressures and high temperature with diluted Xe and krypton (Kr) in air or nitrogen are enriched in heavy Xe isotopes by +0.8 to +2.3‰ per AMU, and strongly enriched in Xe over Kr. The upper +2.3‰ per AMU value is a minimum because quantitative trapping of unreacted Xe, either in bubbles or adsorbed on the samples, is likely. In light of these results, we propose a scenario solving the missing Xe problem that involves multiple magma ocean stage events at the proto-planetary stage, combined with atmospheric loss. Each of these events results in trapping of Xe at depth and preferential retention of its heavy isotopes. In the case of the Earth, the heavy Xe fraction was later added to the secondary CI chondritic atmosphere through continental erosion and/or recycling of a Hadean felsic crust.

Atmospheric Xe is elementally depleted by a factor of 24 relative to Kr in CI chondrites (Table 1), and isotopically depleted by 35 ‰ per AMU, which is known as the missing Xe problem<sup>1</sup>. The loss of elemental Xe occurred very early<sup>4</sup> (<100 Myr). Its isotopic fractionation in the terrestrial atmosphere is recorded continuously throughout the Archean<sup>5</sup>, a situation that settled before 4 Gyr for the Martian atmosphere. Scenarios have been proposed to explain this, but so far none are exempt from ad-hoc hypothesis<sup>6</sup>. Atmospheric escape scenarios<sup>7–9</sup> require strong extreme ultraviolet (EUV) radiation and/or magnetic fields to selectively ionize Xe, amongst other noble gases, by collision with H<sup>+</sup> ions, a sufficiently large H<sub>2</sub> drag and, eventually, an additional Xe-specific process to retain it at depth<sup>7</sup> or in organic aerosols<sup>8</sup>. Atmospheric escape processes should also be related to the mass of the planet, which is not consistent with Mars and Earth having the same missing Xe problem. An alternative scenario to alleviate the need for Xe loss is to have a cometary component in the planetary building blocks<sup>10</sup>. Comets are indeed expected to have much smaller Xe/Kr and Xe/Ar ratios than chondrites, on the basis of noble gas trapping experiments on ice, but this has not been confirmed by analyses from comet 67P/Churyumov–Gerasimenko<sup>11</sup>. Comets are in fact even more enriched in light isotopes than chondrites, compared to the atmosphere<sup>12</sup>. A 22% comet:78% chondrite mix matches the U-Xe component from which the atmospheric Xe isotopic signature is obtained by mass-dependent fractionation, but that does not explain the mass-dependent fractionation process itself. Last, but most importantly, the terrestrial budget of water seems to be better explained by a mostly enstatite chondritic Earth<sup>13</sup>, which satisfies the largest number of geochemical constraints<sup>14,15</sup>, and only a minor late input of carbonaceous chondrites to surficial reservoirs. If the noble gases planetary budget was indeed established very early on, as for water, then the continuous depletion of atmospheric Xe light isotopes throughout the Archean might not necessarily trace

the isotopic fractionation process, but might instead trace the release of a formerly trapped heavy component.

Trapping-at-depth scenarios stem from the effect of high pressures (*P*) to induce Xe chemistry at depth with planetary materials<sup>16</sup>. Xe may covalently bond to oxygen in pure oxides at the pressure–temperature (*P*–*T*) conditions of the lower mantle<sup>17</sup>; it may also bond to nickel at the conditions of the Earth's deep outer core<sup>18</sup>. High *P* phases, however, may only be relevant as a trapping scenario if they include Xe at natural levels of abundance, that is, as a trace element, and not if they are stoichiometric compounds. The fact that Mars and Earth share the missing Xe problem excludes the lower mantle and core as potential reservoirs. Instead, Xe oxidation by substitution to Si in silicates is a viable mechanism. It occurs at the modest *P*–*T* conditions of the deep crust, and higher, in all types of silicates with tetrahedral silicon from isolated tetrahedral olivine<sup>19</sup> to framework quartz<sup>20,21</sup>, and at trace concentrations of Xe with a storage capacity up to 0.4 at%. Unlike for tetrahedrally coordinated silicates, Xe is not retained within the octahedral coordinated silicates of the lower mantle, such as in bridgmanite<sup>22</sup>. Therefore, unlike crustal, upper mantle and atmospheric reservoirs, the lower mantle probably does not currently retain Xe in silicates, except for zones that could have remained isolated from the convecting mantle. Ingassing through subduction recycles Xe at depth<sup>23</sup> by neutral retention in cyclo-silicates in the altered lithosphere<sup>24</sup>, and it is released in the upper mantle along with the aqueous fluid on plate dehydration.

Table 1 summarizes the occurrence of heavy noble gas (Xe/Kr/Ar) enrichments in naturally high *P* samples. Bravo Dome fluids<sup>25</sup> and MORB popping rock value<sup>26</sup> enrichments are partially explained by seawater recycling at depth (Xe/Kr enrichment by a factor of 2) with another source of enrichment, such as added oceanic sedimentary component<sup>25</sup>; although the latter should give other geochemical imprints that are not observed. Mantle xenoliths<sup>27–29</sup> display a stronger

<sup>1</sup>Sorbonne Université, CNRS, Muséum National d'Histoire Naturelle, Institut de Minéralogie, de Physique des matériaux et de Cosmochimie, UMR7590, Paris, France. <sup>2</sup>Université de Bordeaux, CNRS, LP2i Bordeaux, UMR5797, Gradignan, France. ✉e-mail: chrystele.sanloup@sorbonne-universite.fr

Table 1 | Xe/Kr/Ar ratios in natural samples

Sample	$^{130}\text{Xe}/^{84}\text{Kr}$	$^{130}\text{Xe}/^{36}\text{Ar}$	$\left(\frac{^{130}\text{Xe}}{^{84}\text{Kr}}\right)_{\text{sample}} / \left(\frac{^{130}\text{Xe}}{^{84}\text{Kr}}\right)_{\text{air}}$	$\left(\frac{^{130}\text{Xe}}{^{36}\text{Ar}}\right)_{\text{sample}} / \left(\frac{^{130}\text{Xe}}{^{36}\text{Ar}}\right)_{\text{air}}$	$\left(\frac{^{130}\text{Xe}}{^{84}\text{Kr}}\right)_{\text{sample}} / \left(\frac{^{130}\text{Xe}}{^{84}\text{Kr}}\right)_{\text{EH}}$
Air <sup>55</sup>	$5.63 \times 10^{-3}$	$1.17 \times 10^{-4}$	1	1	0.1
CI <sup>6</sup>	0.135	$1.49 \times 10^{-3}$	24	12.5	2.1
EH <sup>11</sup>	0.1	$7.15 \times 10^{-4}$	17.8	6.1	1
<b>Mantle samples</b>					
MORB <sup>26</sup>	$9.25 \times 10^{-3}$	$2.2 \times 10^{-4}$	1.6	1.9	0.3
Bravo Dome fluids <sup>25</sup>	$(1.6\text{--}3.0) \times 10^{-2}$	$(5.3\text{--}7.5) \times 10^{-4}$	<b>(2.8–5.4)</b>	<b>(4.6–6.4)</b>	(0.2–0.3)
Xenoliths <sup>27–29</sup>	$(0.4\text{--}3.8) \times 10^{-2}$	$(0.7\text{--}19.7) \times 10^{-4}$	<b>(0.7–6.7)</b>	<b>(0.6–16.7)</b>	(0.04–0.38)
<b>Felsic crusts</b>					
KTB drilling project <sup>33</sup>	$(1.9\text{--}90.0) \times 10^{-3}$	$(1\text{--}80) \times 10^{-4}$	<b>(0.3–16.0)</b>	<b>(0.8–68.7)</b>	(0.02–0.90)
Red rock impact <sup>30</sup>	0.199	0.163	<b>35.3</b>	<b>1,395.7</b>	<b>2.0</b>
Tektites <sup>31</sup>	0.529	$4.17 \times 10^{-2}$	<b>94.0</b>	<b>357.2</b>	<b>6.4</b>
Lunar anorthosite <sup>32</sup>	$(1.6\text{--}11.9) \times 10^{-2}$	$(1.3\text{--}25.8) \times 10^{-3}$	<b>(2.9–21.1)</b>	<b>(11.1–220.5)</b>	(0.2–1.2)

Heavy noble gas enrichment compared to air and to potential bulk Earth noble gas compositions. Ratios are from abundances given in mol g<sup>−1</sup>. Notable Xe enrichments are given in bold characters.

Xe over Ar enrichment of up to 17 times that of air, albeit that Kr data are not available for these samples<sup>29</sup>. Much stronger Xe enrichments are observed in continental crust samples, by one to two orders of magnitude versus Kr, and two to three orders of magnitude versus Ar, with the strongest values being for impact rocks<sup>30,31</sup>. Similar enrichment values are reported for excavated lunar anorthosites<sup>32</sup>. Relative to the chondritic noble gas concentration trend, 8 to 12 atmospheric masses of Xe are missing<sup>11</sup>, which translates into a <sup>132</sup>Xe concentration of  $1.1 \times 10^{-14}$  mol g<sup>−1</sup> to  $1.7 \times 10^{-14}$  mol g<sup>−1</sup> if stored in the crust and upper mantle. This matches the highest concentrations reported in shocked granite<sup>30</sup> ( $1.3 \times 10^{-14}$  mol g<sup>−1</sup>) and lunar anorthosite<sup>32</sup> (up to  $1.7 \times 10^{-14}$  mol g<sup>−1</sup>), whereas next-highest Xe concentrations are reported for the KTB continental crust drill<sup>33</sup> ( $1.5 \times 10^{-15}$  mol g<sup>−1</sup>) and deep fluids<sup>25</sup> ( $2.5 \times 10^{-15}$  mol g<sup>−1</sup>). Given that Xe is not preserved in the crystal structure of silicates brought back to surface conditions, and is expected to diffuse out on geological timescales, the natural record only gives a minimum estimation of the relevant Xe content at depth. Indeed, Xe content is highest in shocked rocks, that is, rocks brought back to ambient *P* on very short timescales that limit diffusion out. This is also seen in the Xe/Kr ratios, which remain higher than chondritic only in rapidly exhumed shocked rocks<sup>30,31</sup>. The next step is to evaluate what the consequences of Xe retention in silicates are on its isotopic signature.

Here, we report Xe isotopic fractionation of +0.8 to +2.3 ± 0.2‰ per AMU in feldspar and olivine crystals mixed with Xe and Kr diluted in either air or nitrogen gas, and brought to high *P* and *T* conditions of 3.5 GPa and 800 °C to 1,100 °C (Fig. 1 and Extended Data Table 1). Xe isotopic fractionations are measured by mass spectrometry on bulk sample fragments fully melted by laser heating (Methods). This fractionation is observed for both olivine and feldspar, but only in samples undersaturated in Xe, that is, mixed with either 1% or 1‰ Xe and Kr diluted in either air or nitrogen gas. The results do not depend on the nature of the dilution gas, that is, with or without oxygen (Fig. 2a), nor on the sample fragment mass (Extended Data Fig. 1b) or Xe content (Fig. 2b). Considering that Xe was partitioned between the N<sub>2</sub>-rich fluid phase (that is, the pressurized gas) and crystals at high *P* and *T*, and that a fraction of the non-oxidized Xe might be retained by adsorption on grains and/or trapped in bubbles, +2.3‰ per AMU is a lower limit. Attempts to isolate the oxidized Xe fraction by step heating show variations in isotopic fractionation by a factor of two depending on *T* (Extended Data Fig. 2). Hence, the real Xe isotopic fractionation resulting from Xe oxidation in silicates at depth should not exceed +4‰ per

AMU. After recovery at ambient conditions, the heavy Xe fraction is retained in the sample on a scale of up to 400 days after the experiment (Extended Data Fig. 1a). By contrast, samples saturated in Xe, with Xe exsolution in bubbles observed in quenched samples (Extended Data Fig. 3), do not show any isotopic fractionation (Fig. 2a). For these samples, the signal is controlled by excess Xe that did not react with the silicates at high *P* and *T* and is not isotopically fractionated (Extended Data Table 1). For undersaturated samples, the Kr isotope signals are within the background signal so that isotopic ratios could not be quantitatively measured. As Xe and Kr are present in equivalent quantities in the diluted gases, this does however demonstrate that Kr is strongly depleted compared to Xe by two to four orders of magnitude in the reacted minerals. The observed isotopic fractionation results from Xe partitioning between phases with markedly different oxidation states, that is, reduced <sup>0</sup>Xe in the fluid phase and oxidized <sup>+3</sup>Xe<sup>19,21</sup> in high *P*–*T* silicates. Xenon oxidation state in compressed magmas has not yet been determined, and we find no isotopic fractionation for feldspar glasses quenched from the molten state at 1,400 °C and 3.5 GPa (Fig. 2a and Extended Data Table 1), despite being undersaturated in Xe. Combining our results on crystal/N<sub>2</sub>-rich fluid and melt/N<sub>2</sub>-rich fluid systems, Xe isotopic fractionation between crystals and melt is expected to be equal to that measured between crystal and N<sub>2</sub>-rich fluid. The onset of feldspar and olivine crystallization occurred at 0.6 GPa and 3.9 GPa, respectively, in the lunar magma ocean<sup>34</sup>, which can be considered as a good analogy of magma oceans in planetary embryos. Hence, the relevant conditions for Xe trapping at depth and consequent isotopic fractionation are of the order of one to several GPa.

We observe the same level of isotopic and elemental enrichment for both feldspar and olivine in our experimental samples, whereas continental crust-like natural samples show the strongest Xe over Kr enrichment. On the basis of these results, we propose that Xe became trapped and isotopically fractionated on Earth and Mars in tetrahedral silicates (Fig. 3a) preferentially in the primordial felsic crusts as they were formed, and were reworked on meteoritic impacts in the early Hadean, and to a lesser extent in the crystallizing mantle unless the poorly sampled sublithospheric mantle contains more Xe than lithospheric xenoliths (Table 1). There is evidence of felsic crusts in the inner solar system from the planetesimal stage<sup>35</sup> to the planetary stage. The existence of a primordial felsic crust within the first 100 Myr is attested by zircons on Mars<sup>36</sup>, and it may have formed in large quantities on Earth from 4.5 Gyr onwards<sup>37,38</sup>. Whereas the heavy Xe isotope fraction was retained in silicates at depth, the light fraction was let into the

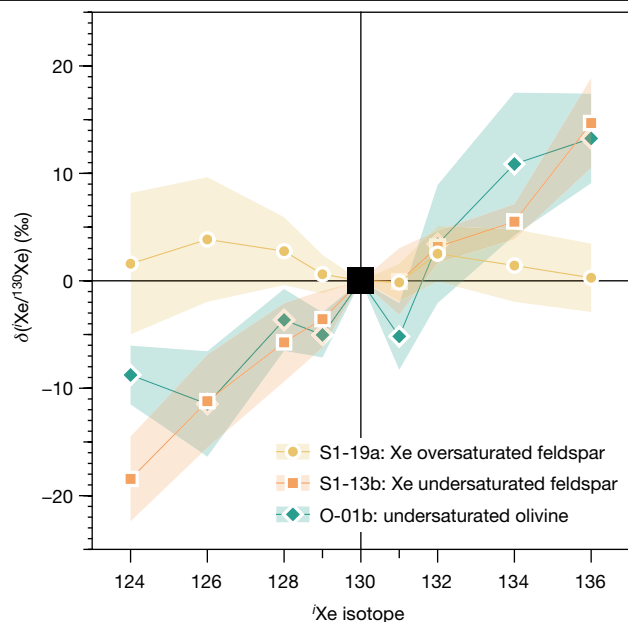


**Fig. 1 | Xenon isotopic spectra.** Feldspar loaded with pure Xe gas (yellow curve, circles), feldspar loaded with 1% Xe and Kr-enriched air (orange curve, squares) and olivine loaded with 1% Xe and Kr-enriched nitrogen (green curve, diamonds); all three samples were brought to 3.5 GPa and 1,100 °C for 24 h. Coloured areas around data points represent the s.e.

atmosphere and was lost by the combination of impacts and EUV-driven hydrodynamic escape within the first 100 Myr (ref. <sup>39</sup>) (Fig. 3b).

With an isotopic fractionation of a few ‰ per AMU on Xe oxidation, the trapping-at-depth process must have occurred not once but multiple times to explain the observed depletion of +35‰ per AMU. In fact, having multiple magma ocean events on the proto-Earth is required to explain the high  $^3\text{He}/^{22}\text{Ne}$  ratio in the MORB mantle source, compared to the 6.7-fold lower solar nebula value, and 11-fold lower chondritic value<sup>40</sup>. Using a  $\text{He}/\text{Ne}$  solubility ratio ( $S_{\text{He}}/S_{\text{Ne}}$ ) of -2 (ref. <sup>41</sup>), magma ocean ingassing of solar nebula gases followed by at least two degassing processes, namely, two magma ocean stages, raises the  $^3\text{He}/^{22}\text{Ne}$  ratio by a factor of  $2 \times 2 \times 2$  (that is, 8), thus satisfying the observations<sup>40</sup>. However, more recent molecular dynamics calculations on noble gas solubility in magmas<sup>42</sup> that include the  $P$  effect predict a  $S_{\text{He}}/S_{\text{Ne}}$  solubility ratio converging to 1.3 at 2,273 K above 2 GPa. Using this value, the minimum number of degassing events is raised to seven. This is still a minimum number<sup>40</sup> as: (1) the  $^3\text{He}/^{22}\text{Ne}$  ratio value of 10 in the MORB source is just a minimum value; (2) atmospheric loss is probably only partial between two successive magma ocean stages; and (3) any deviation from equilibrium degassing or any hydrodynamic escape process at stake would lower the  $^3\text{He}/^{22}\text{Ne}$  ratio. Our results further constrain the number of events between 9 (for  $\delta\text{Xe}^{i+1}/\text{Xe}^i = +4\text{‰}$ ) and 15 (for  $\delta\text{Xe}^{i+1}/\text{Xe}^i = +2.3\text{‰}$ ). The fractionation scenario is therefore a succession of magma oceans and atmospheric loss on proto-planets at the planetary embryo stage while collisions were common<sup>43</sup>, noting that magma oceans and atmospheric loss might not necessarily be concomitant<sup>44</sup>. The similar extent of Xe isotopic fractionation on Earth and Mars implies that Xe isotopic and elemental depletion was settled by the time proto-planets had grown to Mars-size objects. The overall loss of Xe must have been massive, as reported for Ar and Ne<sup>45,46</sup> (that is, of the order of 99% to 99.9%), whereas the ‘missing Xe’ paradox only concerns the relative depletion of Xe compared to Kr and is retained in silicates at depth. Using a Rayleigh distillation law and a depletion of 99.9%, the total +35 ‰/AMU fractionation gives an instantaneous fractionation factor of +5 ‰/AMU. This is very close to the +4 ‰/AMU upper value proposed

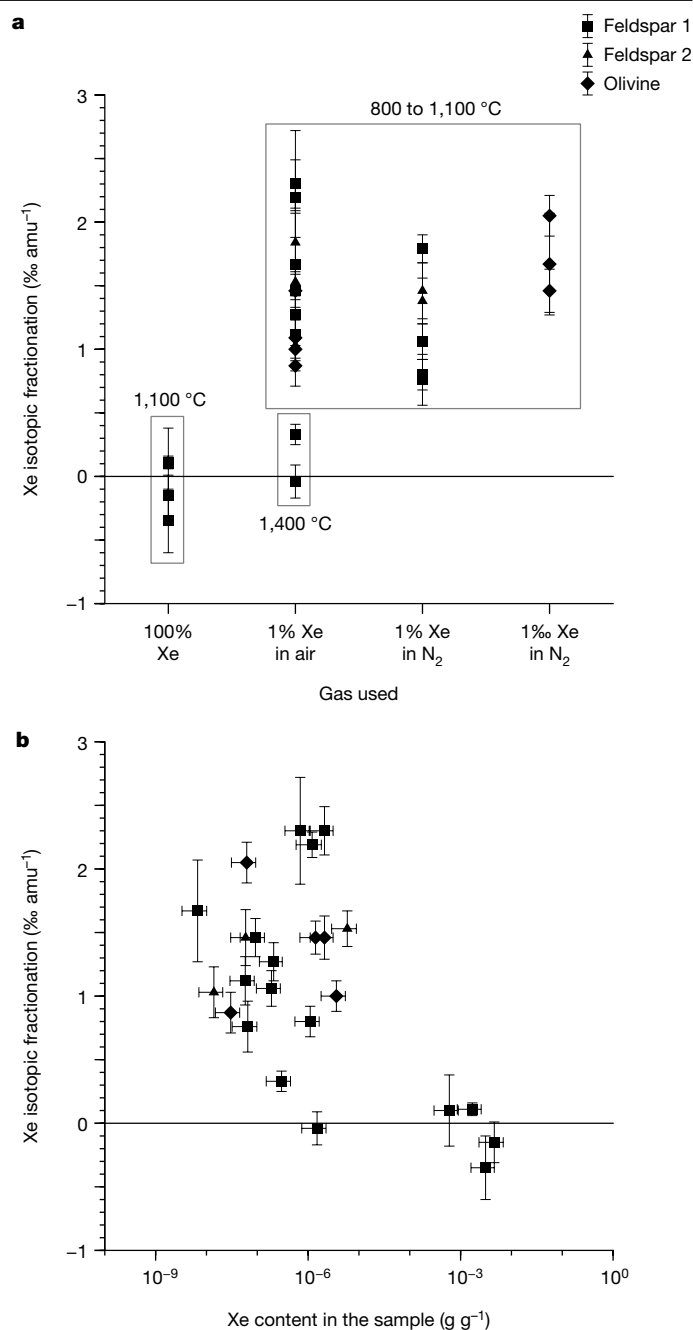


**Fig. 2 | Full Xe isotopic dataset for crystalline feldspar and olivine.** **a**, Xe fractionation as a function of the synthesis gas used (1% and 1‰ represent, respectively, 1 mol% of both Xe and Kr enrichment, and 1 mol‰ of both Xe and Kr enrichment). **b**, Xe fractionation as a function of the sample Xe content. Vertical error bars, s.e.; horizontal error bars on panel **b**,  $\pm 30\%$  error on [Xe] determination. Note that the sample fragment weight was not available for a few data points, hence is not reported in **b** (see Extended Data Table 1).

here. However, this is just an indication, as Xe loss was a combination of continuous hydrodynamic escape processes and erosion impact events, and would therefore require a more complex modelling. Consequently, a lesser mass of late veneer (<0.01% mass Earth) than that based on siderophile elements is required so as not to re-set the fractionated Xe signature. This would also be more consistent with values proposed on the basis of hydrogen isotopes for water<sup>13</sup>, possibly due to the higher volatility of water and noble gases compared to siderophile elements.

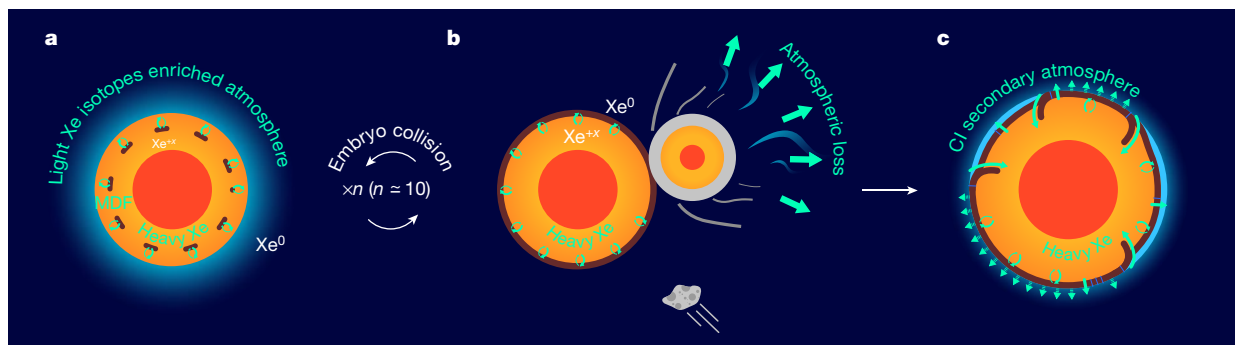


**Fig. 3 | Xe trapping-at-depth scenario.** **a, b**, Due to successive collisions, multiple events of equilibrium between reduced Xe in a primary atmosphere and oxidized Xe in the crystallizing magma ocean, preferential trapping of heavy Xe isotopes at depth in silicates (**a**) and loss of the light isotopic Xe fraction on impact-induced atmosphere erosion and hydrodynamic escape (**b**).

Unlike for Xe, there is no report of *P*-induced oxidation for any other noble gas in crystalline silicates. Oxidation has only been reported for Kr in magmas<sup>47</sup>, with a Kr–O bond length at  $2.5 \pm 0.1 \text{ \AA}$ , which is too large to be accommodated by substitution of Kr to Si in the  $[\text{SiO}_4]^{-4}$  tetrahedra, but which can fit into the melt rings structure<sup>48</sup>. In early planetary stages, Kr bonding to oxygen only in magmas might have resulted in isotopically heavier magmas that eventually degassed before loss of the primary atmosphere, and in isotopically lighter crystals, which is consistent with terrestrial Kr being depleted in heavy isotopes by 0.8‰ per AMU (ref. 49). The Xe/Kr enrichment of two to four orders of magnitude that we measure here confirms the preferential trapping of Xe over lighter noble gases. Literature data on crystal/melt noble gases partitioning are sparse<sup>50</sup>, with values spanning up to six orders of magnitude in the case of Xe from highly incompatible to moderately compatible. Although great care was taken to avoid any melt or bubbles in crystal analyses<sup>50</sup>, Xe bubbles are not necessarily artefacts but can instead be produced on quenching the experiment back to room conditions, as observed in situ X-ray diffraction experiments<sup>51</sup>. Therefore, it is not straightforward to estimate the solubility and partitioning behaviour of noble gases, and, more generally, of volatile elements, from measurements on quenched samples. Ab initio calculations nonetheless confirm the compatibility of Xe in olivine<sup>19</sup>. Consequently, any degassing process from the upper mantle and deep crust is bound to preferentially retain Xe over other noble gases, resulting in the currently observed Xe deficiency in the atmosphere.

The contribution of CI chondrites to the secondary atmosphere later set up the initial atmospheric composition of Xe for the Earth, which was continuously modified by inputs from continents, and through erosion, metamorphic and magmatic processes, until the CI signature became overprinted by released heavy Xe at the end of the Archean (Fig. 3c). At approximately the same time, the Hadean felsic crust would have been well re-mixed with the mantle, as estimated from  $^{142}\text{Nd}$  anomalies<sup>37</sup>. Compared to the early depleted mantle and crust, the enrichment in the light Xe isotopes in the mantle<sup>25,52</sup> reflects either recycling of the more chondritic Archean atmosphere (Extended Data Fig. 4), or input from a slightly less fractionated lower mantle, resulting from the last magma ocean stage having affected only the upper mantle due to the lack of reactivity between Xe and bridgmanite<sup>22</sup>. Mantle degassing has been invoked as a mechanism to release Xe-depleted volatiles following noble gas solubility trends in magmas<sup>53</sup>. Mantle degassing alone cannot explain atmospheric evolution of Xe isotopes, as it occurred on a different timescale with an extensive loss of volatiles within the first 100 Myr (ref. 54). However, recycling of the felsic crust within the mantle and its further degassing by magmatism could have contributed to the evolution of the atmospheric Xe isotopic signature during the Archean<sup>5</sup>.

**c**, Partial release of the trapped heavy Xe in the CI chondritic secondary atmosphere through magmatism/continental erosion during the Archean resulting in an elementally Xe-depleted and isotopically heavy Xe-enriched atmosphere, and Xe ingassing initiated at subduction zones.

## Online content

Any methods, additional references, Nature Research reporting summaries, source data, extended data, supplementary information, acknowledgements, peer review information; details of author contributions and competing interests; and statements of data and code availability are available at <https://doi.org/10.1038/s41586-022-04710-4>.

- Anders, E. & Owen, T. Mars and Earth: origin and abundance of volatiles. *Science* **198**, 453–465 (1977).
- Krummenacher, D., Merrihue, C. M., Pepin, R. O. & Reynolds, J. H. Meteoritic krypton and barium versus the general isotopic anomalies in xenon. *Geochim. Cosmochim. Acta* **26**, 231–249 (1962).
- Swindle, T. D., Caffee, M. W. & Hohenberg, C. M. Xenon and other noble gases in shergottites. *Geochim. Cosmochim. Acta* **50**, 1001–1015 (1986).
- Ozima, M. & Podosek, F. A. Formation age of Earth from  $^{129}\text{I}/^{127}\text{I}$  and  $^{244}\text{Pu}/^{238}\text{U}$  systematics and the missing Xe. *J. Geophys. Res.* **104**, 25493–25499 (1999).
- Avicé, G., Marty, B. & Burgess, R. The origin and degassing history of the Earth's atmosphere revealed by Archean xenon. *Nat. Commun.* **8**, 15455 (2017).
- Dauphas, N. & Morbidelli, A. in *Geochemical and Planetary Dynamical Views on the Origin of Earth's Atmosphere and Oceans* (eds Holland, H. D. & Turekian, K. K.) 115–234 (Elsevier, 2014).
- Pepin, R. O. On the origin and early evolution of terrestrial planet atmospheres and meteoritic volatiles. *Icarus* **92**, 2–79 (1991).
- Hébrard, E. & Marty, B. Coupled noble gas–hydrocarbon evolution of the early Earth atmosphere upon solar UV irradiation. *Earth Planet. Sci. Lett.* **385**, 40–48 (2014).
- Zahnle, K. J., Gaseca, M. & Catling, D. C. Strange messenger: a new history of hydrogen on Earth, as told by xenon. *Geochim. Cosmochim. Acta* **244**, 56–85 (2019).
- Dauphas, N. The dual origin of the terrestrial atmosphere. *Icarus* **165**, 326–333 (2003).
- Bekaert, D. V., Bradley, M. W. & Marty, B. The origin and fate of volatile elements on Earth revisited in light of noble gas data obtained from comet 67P/Churyumov–Gerasimenko. *Sci. Rep.* **10**, 5796 (2020).
- Marty, B. et al. Xenon isotopes in 67P/Churyumov–Gerasimenko show that comets contributed to Earth's atmosphere. *Science* **356**, 1069–1072 (2017).
- Piani, L. et al. Earth's water may have been inherited from material similar to enstatite chondrite meteorites. *Science* **50**, 1110–1113 (2020).
- Javoy, M. et al. The chemical composition of the Earth: enstatite chondrite models. *Earth Planet. Sci. Lett.* **293**, 259–268 (2010).
- Boyett, M. et al. Enstatite chondrites EL3 as building blocks for the Earth: the debate over the  $^{146}\text{Sm}$ – $^{142}\text{Nd}$  systematics. *Earth Planet. Sci. Lett.* **214**, 427–442 (2018).
- Sanloup, C. Noble gas reactivity in planetary interiors. *Front. Phys.* **8**, 157 (2020).
- Dewaele, A. et al. Synthesis and stability of xenon oxides  $\text{Xe}_2\text{O}_5$  and  $\text{Xe}_3\text{O}_2$  under pressure. *Nat. Chem.* **8**, 784–790 (2016).
- Stavrou, E. et al. Synthesis of xenon and iron–nickel intermetallic compounds at Earth's core thermodynamic conditions. *Phys. Rev. Lett.* **120**, 096001 (2018).
- Crépeau, C., Blanchard, M., Lazzeri, M., Balan, E. & Sanloup, C. New constraints on Xe incorporation mechanisms in olivine from first-principles calculations. *Geochim. Cosmochim. Acta* **222**, 146–155 (2018).
- Probert, M. I. J. An ab initio study of xenon retention in  $\alpha$ -quartz. *J. Phys. Condens. Matter* **22**, 025501 (2010).
- Crépeau, C. et al. The Xe– $\text{SiO}_2$  system at moderate pressure and high temperature. *Geochem. Geophys. Geosyst.* **20**, 992–1003 (2019).
- Shcheka, S. S. & Keppler, H. The origin of the terrestrial noble-gas signature. *Nature* **490**, 531–535 (2012).
- Parai, R. & Mukhopadhyay, S. Xenon isotopic constraints on the history of volatile recycling into the mantle. *Geochim. Cosmochim. Acta* **560**, 223–227 (2018).

24. Krantz, J. A., Parman, S. W. & Kelley, S. P. Recycling of heavy noble gases by subduction of serpentinite. *Earth Planet. Sci. Lett.* **521**, 120–127 (2019).
25. Holland, G. & Ballentine, C. J. Seawater subduction controls the heavy noble gas composition of the mantle. *Nature* **441**, 186–191 (2006).
26. Moreira, M., Kunz, J. & Allègre, C. Rare gas systematics in popping rock: isotopic and elemental compositions in the upper mantle. *Science* **279**, 1178–1181 (1998).
27. Hennecke, E. W. & Manuel, O. K. Noble gases in Hawaiian xenolith. *Nature* **257**, 778–780 (1975).
28. Poreda, R. J. & Farley, K. A. Rare gases in Samoan xenoliths. *Earth Planet. Sci. Lett.* **113**, 129–144 (1992).
29. Czuppon, G., Matsumoto, T., Handler, M. R. & Matsuda, J.-I. Noble gases in spinel peridotite xenoliths from Mt Quincan, North Queensland, Australia: undisturbed MORB-type noble gases in the subcontinental lithospheric mantle. *Chem. Geol.* **266**, 19–28 (2009).
30. Kuroda, P. K., Sherrill, R. D. & Jackson, K. C. Abundances and isotopic compositions of rare gases in granites. *Geochim. J.* **11**, 75–90 (1977).
31. Palma, R. L., Rao, M. N., Rowe, M. W. & Koeberl, C. Krypton and xenon fractionation in North American tektites. *Meteor. Planet. Sci.* **32**, 9–14 (1997).
32. Bekaert, D. V., Avice, G., Marty, B. & Henderson, B. Stepwise heating of lunar anorthosites 60025, 60215, 65315 possibly reveals an indigenous noble gas component on the Moon. *Geochim. Cosmochim. Acta* **218**, 114–1315 (2017).
33. Drescher, J., Kirsten, T. & Schäfer, K. The rare gas inventory of the continental crust, recovered by the KTB Continental Deep Drilling project. *Earth Plan. Sci. Lett.* **154**, 247–263 (1998).
34. Elkins-Tanton, L. T., Burgess, S. & Yin, Q.-Z. The lunar magma ocean: reconciling the solidification process with lunar petrology and geochronology. *Earth Planet. Sci. Lett.* **304**, 326–336 (2011).
35. Frossard, P., Boyet, M., Bouvier, A., Hammouda, T. & Monteux, J. Evidence for anorthositic crust formed on an inner solar system planetesimal. *Geochim. Persp. Lett.* **11**, 28–32 (2019).
36. Bouvier, L. C. et al. Evidence for extremely rapid magma ocean crystallization and crust formation on Mars. *Nature* **558**, 586–589 (2018).
37. Caro, G., Bourdon, B., Birck, J.-L. & Moorbath, S. High-precision  $^{142}\text{Nd}/^{144}\text{Nd}$  measurements in terrestrial rocks: constraints on the early differentiation of the Earth's mantle. *Geochim. Cosmochim. Acta* **70**, 164–191 (2006).
38. Harrison, T. M., Schmitt, A. K., McCulloch, M. T. & Lovera, O. M. Early ( $\geq 4.5$  Ga) formation of terrestrial crust: Lu–Hf,  $\delta^{18}\text{O}$ , and Ti thermometry results for Hadean zircons. *Earth Planet. Sci. Lett.* **268**, 476–486 (2008).
39. Erkaev, N. V. et al. Escape of the martian protoatmosphere and initial water inventory. *Planet. Space Sci.* **98**, 106–119 (2014).
40. Tucker, J. M. & Mukhopadhyay, S. Evidence for multiple magma ocean outgassing and atmospheric loss episodes from mantle noble gases. *Earth Planet. Sci. Lett.* **393**, 254–265 (2014).
41. Jambon, A., Weber, H. & Braun, O. Solubility of He, Ne, Ar, Kr and Xe in a basalt melt in the range 1250–1600°C. Geochemical implications. *Geochim. Cosmochim. Acta* **50**, 401–408 (1986).
42. Guillot, B. & Sator, N. Noble gases in high-pressure silicate liquids: a computer simulation study. *Geochim. Cosmochim. Acta* **80**, 51–69 (2012).
43. Brož, M., Chrenko, O., Nesvorný, D. & Dauphas, N. Early terrestrial planet formation by torque-driven convergent migration of planetary embryos. *Nat. Astron.* **5**, 898–902 (2021).
44. Schlichting, H. E. & Mukhopadhyay, S. Atmosphere impact losses. *Space Sci. Rev.* **214**, 34 (2018).
45. Harper, C. L. Evidence for  $^{92}\text{qNb}$  in the early solar system and evaluation of a new  $p$ -process cosmochronometer from  $^{92}\text{Nb}/^{92}\text{Mo}$ . *Astrophys. J.* **466**, 437–456 (1996).
46. Jaupart, E., Charnoz, S. & Moreira, M. Primordial atmosphere incorporation in planetary embryos and the origin of neon in terrestrial planets. *Icarus* **293**, 199–205 (2017).
47. Crépeau, C. et al. Kr environment in feldspathic glass and melt: a high pressure, high temperature X-ray absorption study. *Chem. Geol.* **493**, 525–531 (2018).
48. Kohara, S. et al. Relationship between topological order and glass forming ability in densely packed enstatite and forsterite composition glasses. *Proc. Natl Acad. Sci. USA* **108**, 14780–14785 (2011).
49. Holland, G., Cassidy, M. & Ballentine, C. J. Meteorite Kr in Earth's mantle suggests a late accretionary source for the atmosphere. *Science* **326**, 1522–1525 (2009).
50. Heber, V. S., Brooker, R. A., Kelley, S. P. & Wood, B. J. Crystal-melt partitioning of noble gases (helium, neon, argon, krypton, and xenon) for olivine and clinopyroxene. *Geochim. Cosmochim. Acta* **71**, 1041–1061 (2007).
51. Sanloup, C., Schmidt, B. C., Gudfinnsson, G., Dewaele, A. & Mezouar, M. Xenon and argon: a contrasting behavior in olivine at depth. *Geochim. Cosmochim. Acta* **75**, 6271–6284 (2011).
52. Péron, S. & Moreira, M. Onset of volatile recycling into the mantle determined by xenon anomalies. *Geochim. Persp. Lett.* **9**, 21–25 (2018).
53. Tolstikhin, I. N. & O'Nions, R. K. The Earth's missing xenon: a combination of early degassing and of rare gas loss from the atmosphere. *Chem. Geol.* **115**, 1–6 (1994).
54. Yokochi, R. & Marty, B. Geochemical constraints on mantle dynamics in the Hadean. *Earth Planet. Sci. Lett.* **238**, 17–30 (2005).
55. Sano, Y., Marty, B. & Burnard, P. in *Noble Gases in the Atmosphere* (ed. Burnard, P.) 17–31 (Springer-Verlag, 2013).

**Publisher's note** Springer Nature remains neutral with regard to jurisdictional claims in published maps and institutional affiliations.

© The Author(s), under exclusive licence to Springer Nature Limited 2022



## Methods

### Sample preparation

Samples were made from mortar-crushed natural mineral powders, namely olivine from a San Carlos peridotite, and two feldspar sanidine samples, one from an unknown location (sanidine 1) and one from Itrongay in Madagascar (sanidine 2). Extended Data Table 2 reports the composition of the three minerals<sup>56,57</sup>. The powder was put into a platinum (Pt) tube enclosed at one side only and was gas loaded<sup>58</sup> with air or nitrogen enriched in both Xe and Kr. Xe and Kr contents were 1‰ or 1% for undersaturated conditions (Air Liquide gas bottles). For oversaturated conditions, pure Xe was used. The Pt capsules were 5 mm tall and 3 mm wide, and were inserted in pairs in a 10 mm diameter talc-Pyrex cell assembly. High  $P$ – $T$  conditions of 3.5 GPa and up to 1,400 °C were generated by a Depth of the Earth L.L.C. piston cylinder press. Run duration varied from 2 to 72 h, depending on the run temperature (Extended Data Table 1).

Starting and recovered samples from high  $P$ – $T$  experiments were embedded in an epoxy resin slab for scanning electronic microscopy (SEM) observations, and electron probe micro-analysis (EPMA). SEM was used with its angle-selective detector (AsB). EPMA (Extended Data Table 2) was performed using the SX-Five quintuple spectrometer device on the CAMPARIS platform. The beam size was 1 µm. Samples were all gas loaded with a gas pressure of 12 bar. However, the amount of gas effectively loaded in capsules varied due to the capsule sealing process, during which part of the loaded gas may escape. SEM images (Extended Data Fig. 3) show the range of textures observed for sanidine 1 samples, from bubble-free (Extended Data Fig. 3a) to bubble-rich (Extended Data Fig. 3b, c), depending on the amount of gas loaded.

### Isotopic ratio measurements

Isotopic ratios were measured at LP2i (formerly CENBG) on the Pia-gara platform (interdisciplinary platform for noble gas analysis), and all data are provided in the Supplementary Information file, along with Xe isotope spectra for each analysis. Pieces of samples from 0.1 mg to 3.3 mg were weighted preferentially using a CAHN/Ventron 21 automatic electrobalance with an accuracy of about 1%, or a Mettler–Toledo ME204 balance with an accuracy of 0.1 mg. Each piece was then placed in a cavity shaped in a tantalum (Ta) sheet, which was itself supported by a tungsten (W) cylinder. The Ta sheet and W support were previously heated up to approximately 2,100 K to ensure the removal of any eventual trapped gas. The sample and its support were put in a degassing chamber and pumped overnight, reaching a residual pressure below  $10^{-8}$  mbar. Sample heating was achieved by focusing a high-power continuous-wave laser<sup>59</sup> while working in a relatively cold environment (chamber walls, base and viewport not exceeding 150 °C), and continuously monitored by a camera until full melting was reached, as attested by the sample shape changing to a spheroid and the simultaneous release of micro-bubbles of gas. Laser power was held steady for a further 30 s, and then shut down. The extracted gases were subjected to a 10 min treatment with hot Ti sponges to remove all non-noble gases. This purification step was completed on the gas fraction brought to the mass spectrometer (MS) by an additional 10 min treatment on a second set of Ti sponges set at 300 °C, 400 °C, 500 °C and 600 °C, and a SORB-AC trap (SAES Getter). A second SORB-AC trap was also present in the MS volume. The MS used for the analyses was a magnetic sector, 60° deflection and 12 cm radius instrument (model 1202 of V. G. Micromass 12) incorporating a small interior volume, a Nier-type source (VG3000) and a (Cu-Be) electron multiplier detector and used in integrating mode for ion counting.

The isotopic fractionations being sought were expected to be extremely low, so extensive care has to be taken to ensure the validity and improve the precision of the values determined. Our magnetic sector mass spectrometer, as for all such instruments, has a sensitivity,  $s_i$  for each isotope  $i$  that will evolve with time and depends on numerous

parameters, most notably gas pressure (total, and that of the considered element and isotope). Consequently, we routinely considered  $s_i$  to be known with a 5% error with a recent calibration, which is two orders of magnitude more than the precision we needed for the present study. Although this error was reduced by one order of magnitude when considering isotope ratios of the same element, a mass discrimination factor correction with its own error and influencing parameters still needs to be applied, as the heavier the isotope, the lower the sensitivity. Therefore, to further lower the intrinsic error on the  $^{i}\text{Xe}/^{130}\text{Xe}$  ratios (with  $^{130}\text{Xe}$  being arbitrarily selected as the reference isotope), we defined the measured ratio  $R_i$  as follows:

$$R_i = \frac{\left( I_i^{\text{sample}} \times \frac{s_i^{\text{sample}}}{s_{130}^{\text{sample}}} \right)}{\left( r_i^{\text{com.gas}} \times \frac{s_i^{\text{com.gas}}}{s_{130}^{\text{com.gas}}} \right)} \quad (1)$$

with  $r = ^i\text{Xe}/^{130}\text{Xe}$ , determined by the time-zero regression of the ratio of the electrical currents  $I_i$  and  $I_{130}$  measured by the MS detector for the  $^i\text{Xe}$  and  $^{130}\text{Xe}$  isotopes, and ‘com.gas’ an aliquot of the Air Liquide gas used for the sample synthesis at high  $P$  and  $T$ . Measuring Xe MS intensity ratios from the reference synthesis gas, and sequentially later (or earlier) on the same day that extracted out of the fused sample with optimally less than a 10% difference in the Xe quantities between the two analysed aliquots, enabled us to cancel out sensitivities ( $s$ ) from equation (1) ( $s_i^{\text{com.gas}} = s_i^{\text{sample}}$  and  $s_{130}^{\text{com.gas}} = s_{130}^{\text{sample}}$ ). This simplifies to:

$$R_i = \frac{\left( \frac{I_i^{\text{sample}}}{I_{130}^{\text{sample}}} \right)}{\left( \frac{I_i^{\text{com.gas}}}{I_{130}^{\text{com.gas}}} \right)} \quad (2)$$

Each  $r_i^{\text{sample}}$  of a sample fragment was obtained from a sole MS run (except for  $i = 134$  or 136, see Supplementary Information) and  $r_i^{\text{com.gas}}$  was only determined from an also unique com.gas measurement made the same day under conditions as close as possible to that of the sample. As such, our data errors originate from in-run standard errors (s.e.) or  $r_i$  measurements and are propagated to the relevant isotopic fractionation values according to customary error quadratic propagation rules<sup>60</sup>. With this protocol,  $R_i$  uncertainties range from 1‰ to 10‰, with uncertainty levels mostly related to the relative abundance of the considered isotope. The individual fractionation  $\delta_i$  was then directly derived from  $R_i$ :  $\delta_i = 1,000 \times (R_i - 1)$ , with  $\delta_i$  expressed in ‰ per AMU. The average fractionation  $\delta_n$  was finally obtained by linear regression with error weighting using the OriginLab 2016 software. Each  $\delta_i$  of a series contributes to the linear regression allowing  $\delta_n$  determination proportionally to  $1/\sigma_i^2$  with  $\sigma_i$  the standard error associated with  $\delta_i$  (propagated from the standard error associated with the MS measurements). All of the  $r_i$ ,  $R_i$ ,  $\delta_i$  and  $\delta_n$  values with associated uncertainties are provided in the Supplementary Information. Given the uncertainties associated with the isotopic ratio measurements, the protocol used enables us to consider any  $\delta_n$  value  $\geq 0.5$  ‰ per AMU as proof of a real fractionation.

### Data availability

All data generated or analysed during this study are included in this published article and its supplementary information file, and are available on the Zenodo repository (<https://doi.org/10.5281/zenodo.6076901>). Source data are provided with this paper.

56. Crépissin, C. ‘Missing Xenon’: Experimental and Theoretical Study of Xe Storage in Crustal and Upper Mantle Minerals. Ph.D. thesis, Sorbonne Univ. (2018).
57. Prouteau, G., Scaillet, B., Pichavant, M. & Maury, R. Evidence for mantle metasomatism by hydrous silicic melts derived from subducted oceanic crust. *Nature* **410**, 197–200 (2001).

58. Boettcher, S. L., Guo, Q. & Montana, A. A simple device for loading gases in high-pressure experiments. *Am. Mineral.* **74**, 1383–1384 (1989).
59. Horlait, D. et al. A new thermo-desorption laser-heating setup for studying noble gases diffusion and release from materials at high temperatures. *Rev. Sci. Instr.* **92**, 124102 (2021).
60. Bevington, P. R. & Robinson, D. K. *Data Reduction and Error Analysis for Physical Sciences* 3rd edn (McGraw-Hill, 2003).

**Acknowledgements** The research leading to these results was funded by the French CNRS PRIME80 and CNRS MITI Défi ISOTOP programmes. We acknowledge B. Lavielle and D. Bekaert for insightful discussions, R. Faure and B.A. Thomas for their technical assistance on MS measurements and T. Chematinov for his useful and appreciated participation in carrying out the step heating experiments. SEM measurements were done at the FIB and SEM facility at IMPMC, supported by Région Ile de France grant SESAME 2006 N°I-07-593/R, and by the French National Research Agency (ANR) grant no. ANR-07-BLAN-0124-01. We acknowledge G.

Prouteau for providing the San Carlos olivine samples, and the mineralogical collection at Sorbonne Université for providing the feldspar samples.

**Author contributions** C.S. and D.H. devised the project, I.R. and C.S. carried out the high *P-T* experiments, I.R., D.H. and E.G. carried out analyses on the noble gas spectrometer. C.S. wrote the paper with input from I.R. and D.H.

**Competing interests** The authors declare no competing interests.

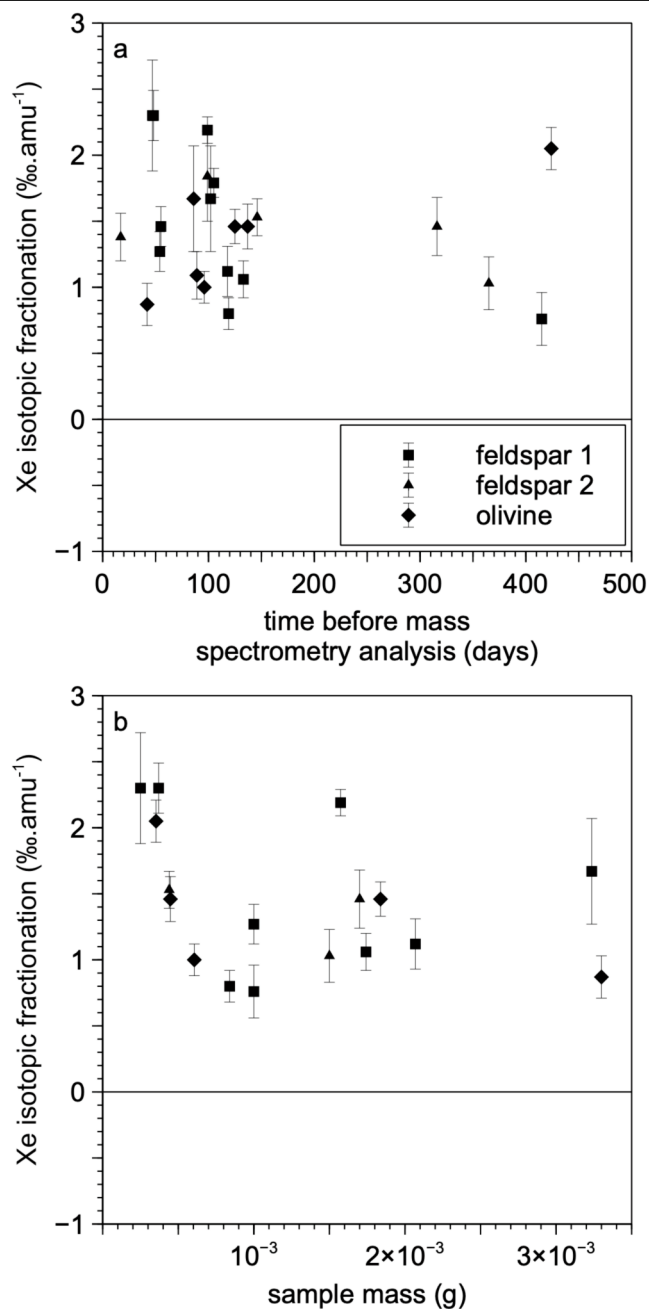
#### **Additional information**

**Supplementary information** The online version contains supplementary material available at <https://doi.org/10.1038/s41586-022-04710-4>.

**Correspondence and requests for materials** should be addressed to Chrystèle Sanloup.

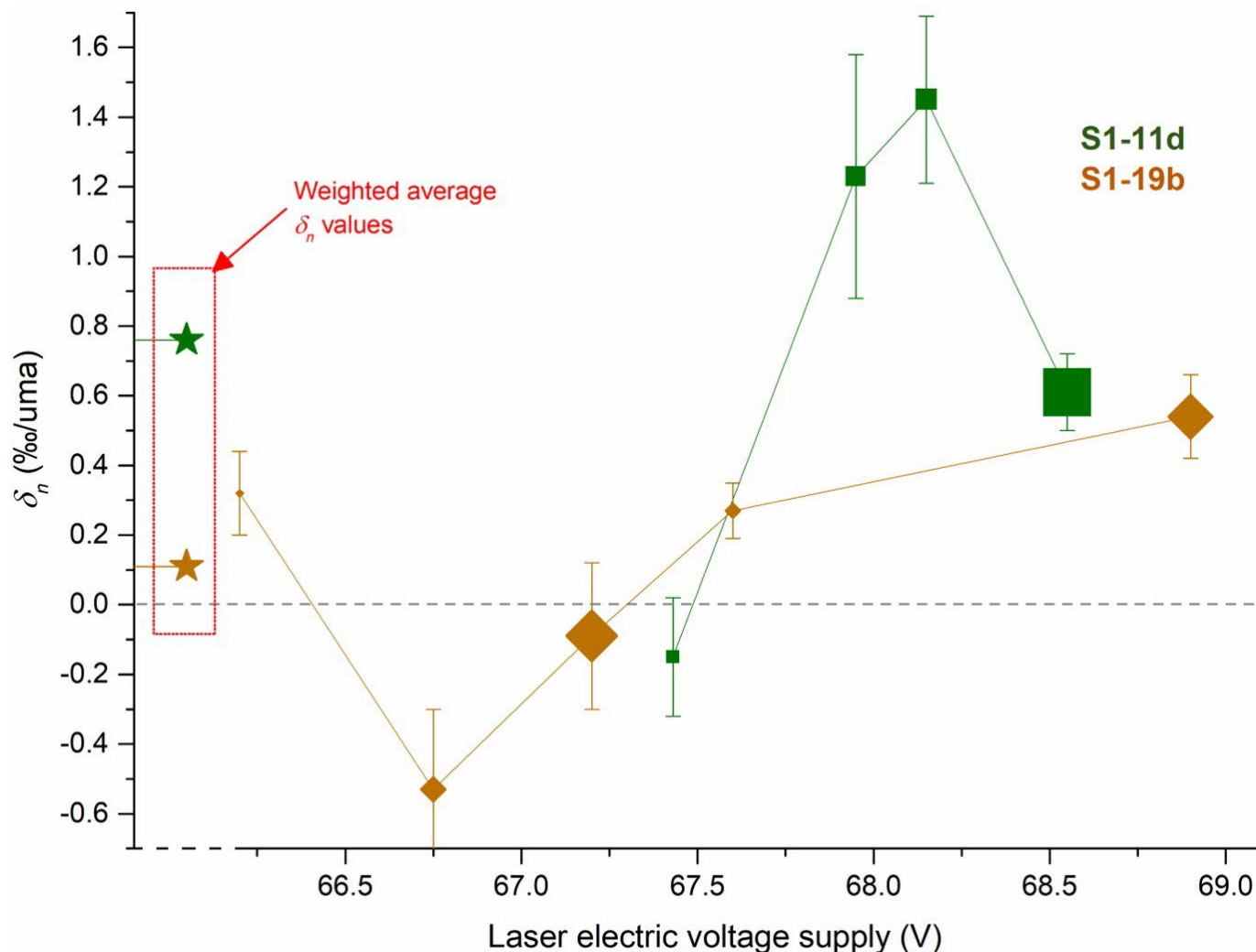
**Peer review information** *Nature* thanks Ray Burgess and the other, anonymous, reviewer(s) for their contribution to the peer review of this work. Peer reviewer files are available.

**Reprints and permissions information** is available at <http://www.nature.com/reprints>.



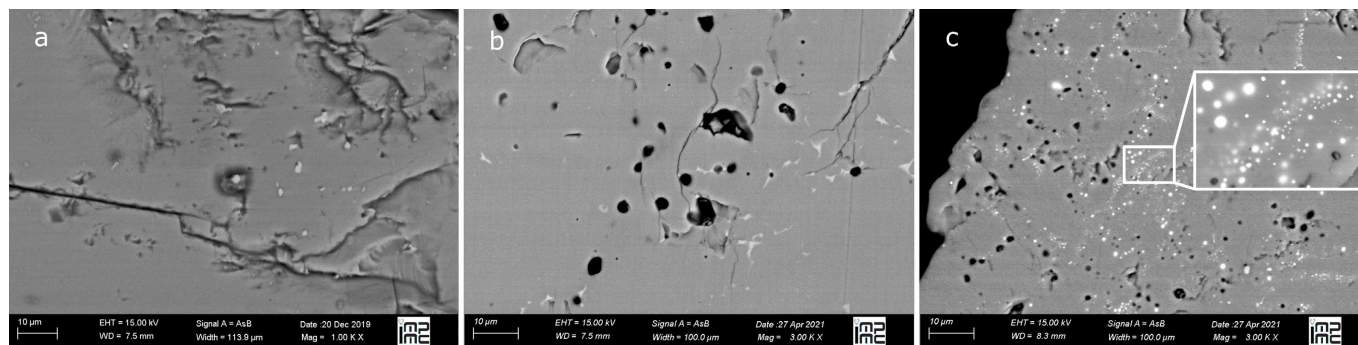
**Extended Data Fig. 1 | a, Xe fractionation as a function of the time spent between the synthesis and the mass spectrometry analysis, and b, Xe fractionation as a function of the sample mass.** Data points for samples characterized, as expected, by an absence of detectable fractionation (runs at 1,400 °C or with 100% Xe loading gas) were removed from this Figure for the sake of clarity. Vertical error bars represent the SE for isotopic fractionation calculation.





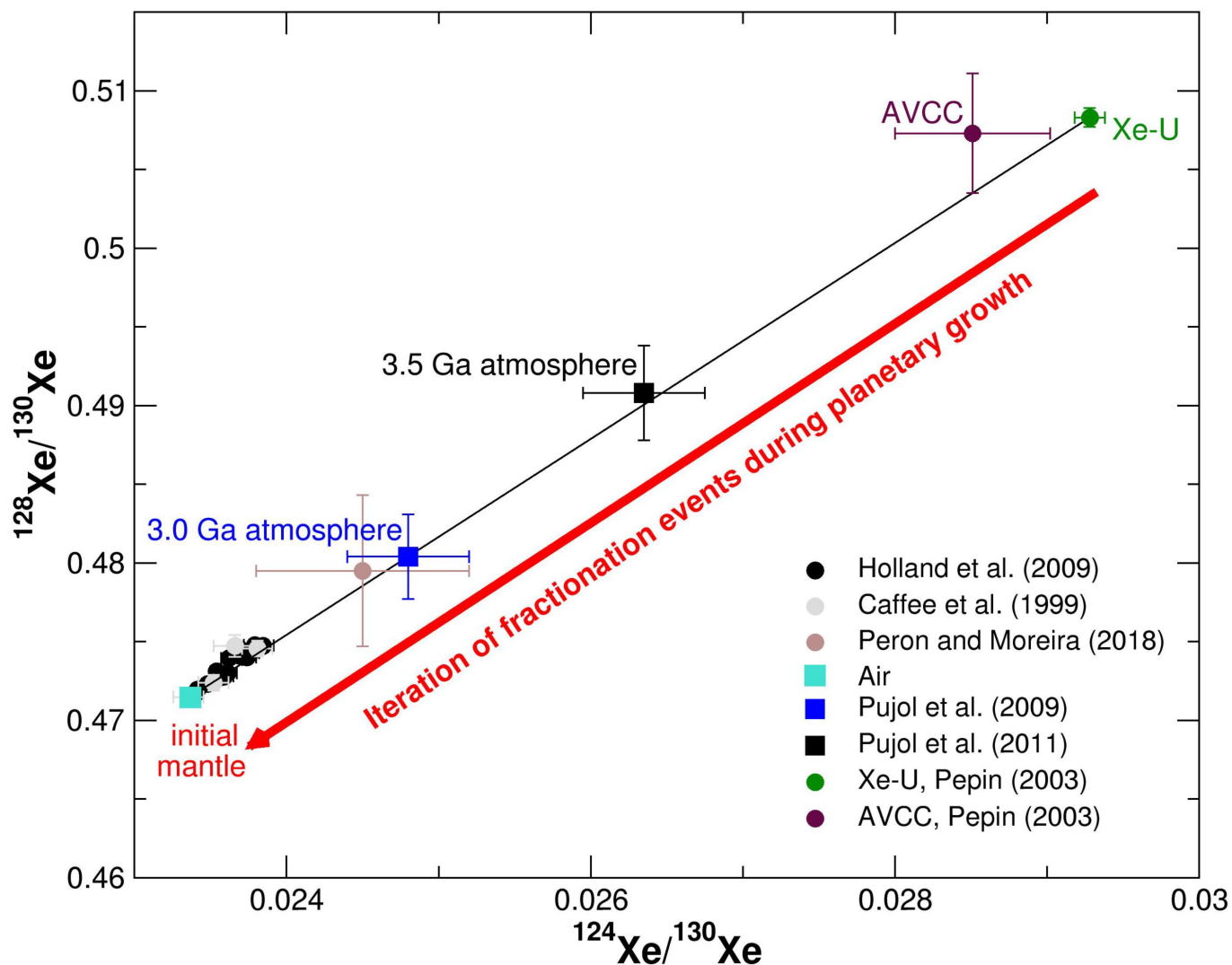
**Extended Data Fig. 2 | Summary of measured  $\delta_n$  values in experiments realized with laser heating increasing steps.** Instead of analysing all Xe released after laser melting of the fragments, the tuneable heating laser was first set at lower powers (indicated as the power voltage V applied to the laser source). Each heating plateau was kept for a few minutes and the released Xe were analysed by mass spectrometry using the same general protocol described in the Methods section. A handful attempts were made on olivine and sanidine 1 samples. They all point toward Xe predominantly exiting the material at the fusion point (or close to). Only two experiments with sanidine, S1-11d with 1%Xe gas and S1-19b with 100%Xe gas, led to the successful measurement for all of the heating steps of both  $\delta_n$  and [Xe] values, as reported in the present Figure. Each point area is proportional to the Xe content ([Xe]) extracted at the heating plateau. The stars are  $\delta_n$  values combining all  $\delta_n$  measured and weighted by each [Xe], in other words the  $\delta_n$  we would had measured if the sample fragment had been directly melted. For S1-11d (1% Xe gas), we observe variations of  $\delta_n$  by a roughly 2-fold factor along the heating

ramp. For this same sample, an unfractionated component was evidenced for the lowest laser voltage, but represent a marginal part (5.3% of the total released Xe). Since for similar heating power, ~45% of the total Xe of S1-19b (100% Xe gas) was released, this low  $T$  release is possibly associated to Xe trapped as bubbles. At the highest  $T$ , i.e. at the sample melting point, for S1-19b and S1-11d respective  $0.54 \pm 0.12$ ‰/amu and  $0.61 \pm 0.11$ ‰/amu fractionations were measured, which points towards a Xe component with some fractionated Xe, but still with an unfractionated component lowering the overall measured  $\delta_n$ . This indirectly confirms that Xe chemical incorporation and the associated isotopic fractionation occurs in all samples prepared at  $T \leq 1,100$  °C;  $\delta_n$  close to zero for samples prepared with 100% Xe gas being only due to a disruptive phenomenon whose extent is proportional to Xe partial pressure: oversaturation of the mineral (bubble formation, as seen in Extended Data Fig. 3). Detailed data used to construct this Figure are found in the results Tables for S111d and S1-19b given in Supplementary information file, while synthesis conditions are found in Extended Data Table 1.



**Extended Data Fig. 3 | SEM images in AsB mode. a and b,** Feldspar sanidine 1 loaded with 1 mol% Xe and 1 mol% Kr enriched air (identical to syntheses S1–13 and S1–14). Round dark area in **b** are synthesis gas bubbles revealed and opened

by polishing. **c,** a sanidine 1 loaded with 100 mol% Xe (identical to syntheses S1–17, S1–18 and S1–19). Brighter areas in **c** are Xe bubbles, found in oversaturated samples, *i.e.* loaded with 100 mol% Xe gas.



**Extended Data Fig. 4 | Non-radiogenic Xe data reveal the possibility of Archean atmosphere contribution to mantle Xe within the present scenario of an early fractionated silicate Earth.** Xe measured in deep crustal fluids<sup>49</sup> (black and grey circles), MORB popping rock<sup>52</sup> (brown circle), air<sup>55</sup>, Archean atmosphere as trapped in crustal samples (dark blue and black

squares); and primordial components (green and maroon circles). All data are shown with associated SE. Alternatively, the deep fluids and MORB popping rock enrichment in Xe light isotopes compared to air could be explained by input from a slightly less fractionated lower mantle resulting from the last magma ocean stage having affected only the upper mantle.

Extended Data Table 1 | Summary of all experimental synthesis runs, Xe contents and average fractionations

Material	Noble gas content and carrier gas	Synthesis T. <i>run duration</i> (°C - <i>hours</i> )	Mass Spec. Analysis # (to refer to individual Tables)	Xe concentration (g/g) ; error: ±30%	Average fractionation δ <sub>n</sub> (‰/amu)
Olivine San Carlos	0.1% Kr + 0.1%Xe in N <sub>2</sub>	1100 - 24	O-01a	2.10 <sup>-6</sup>	1.46 ±0.17
			O-01b (*)	N/D	1.67 ±0.40
			O-01c	6.10 <sup>-8</sup>	2.05 ±0.16
	O-02a		N/D	1.09 ±0.18	
	O-02b		1.5.10 <sup>-6</sup>	1.46 ±0.13	
	O-03		4.10 <sup>-6</sup>	1.00 ±0.12	
	1%Kr + 1%Xe in N <sub>2</sub> with 20%O <sub>2</sub>	800 - 24	O-04	3.10 <sup>-8</sup>	0.87 ±0.16
Sanidine 1	1% Kr + 1% Xe in N <sub>2</sub> with 20% O <sub>2</sub>	1100 - 24	S1-11a	N/D	1.79 ±0.11
			S1-11b	2.10 <sup>-7</sup>	1.06 ±0.14
			S1-11c	1.10 <sup>-6</sup>	0.80 ±0.12
			S1-11d	6.5.10 <sup>-8</sup>	0.76 ±0.20
		1400 - 2	S1-12a	1.5.10 <sup>-6</sup>	-0.04 ±0.13
			S1-12b	3.10 <sup>-7</sup>	0.33 ±0.08
		1100 - 24	S1-13a	7.10 <sup>-7</sup>	2.30 ±0.42
			S1-13b (*)	2.10 <sup>-6</sup>	2.30 ±0.19
	900 - 7 to 17 <sup>†</sup>	S1-14	7.10 <sup>-9</sup>	1.67 ±0.27	
		S1-15a	1.3.10 <sup>-6</sup>	2.19 ±0.10	
		S1-15b	6.10 <sup>-8</sup>	1.12 ±0.19	
		800 - 72	S1-16a	2.10 <sup>-7</sup>	1.27 ±0.15
	S1-16b		9.10 <sup>-8</sup>	1.46 ±0.15	
	Xe 100%	1100 - 24	S1-17	6.10 <sup>-4</sup>	0.10 ±0.28
			S1-18	3.10 <sup>-3</sup>	-0.35 ±0.25
			S1-19a (*)	2.5.10 <sup>-3</sup>	-0.15 ±0.16
S1-19b			1.7.10 <sup>-3</sup>	0.11 ±0.10	
Sanidine 2 (Itrongay)	1% Kr + 1% Xe in N <sub>2</sub>	1100 - 24	S2-21a	N/D	1.38 ±0.18
			S2-21b	4.10 <sup>-8</sup>	1.46 ±0.22
	S2-22a		1.4.10 <sup>-8</sup>	1.03 ±0.20	
	S2-22b		N/D	1.84 ±0.34	
	S2-22c		6.10 <sup>-6</sup>	1.53 ±0.14	

Samples are referred to by their material (O, S1 or S2), their synthesis number (2 digits) and when relevant their fragment number (a single letter). (\*) symbol is used to indicate the results chosen to appear in the main manuscript's Fig. 1. <sup>†</sup>: For S1-15 synthesis, a failure of the cooling water system automatically stopped the run overnight, thus the exact duration of this run could not be determined. Brown writing refer to experimental conditions that led to the absence of detectable fractionation (100% Xe gas leading to sample saturation with Xe bubbles ; runs at 1,400°C resulting in full melting of the mineral). For a few experiments (N/D in the Xe concentration column), the melted fragments were not weighted because of a long unavailability of the microbalance, thus preventing Xe concentration determination. All 29 mass spectrometry results are detailed in individual Tables (Supplementary Information file). Xe contents errors are 99% confidence intervals. Errors associated to the average fractionations  $\delta_n$  are described with the presentation of individual Tables.

Extended Data Table 2 | Chemical composition of starting and recovered samples

Material	S1 (sanidine 1)	S2 (sanidine 2)	O (olivine San Carlos)	S1-13
Na <sub>2</sub> O	5.41 ±1.57	1.82 ±0.09	/	5.59 ±0.39
MgO	0.00 ±0.01	0.00 ±0.01	47.80	0.00 ±0.01
SiO <sub>2</sub>	65.96 ±1.31	64.98 ±0.93	40.80	66.46 ±2.07
Al <sub>2</sub> O <sub>3</sub>	19.91 ±1.78	19.09 ±0.13	0.10	19.44 ±0.57
K <sub>2</sub> O	8.78 ±3.53	14.04 ±0.20	/	9.42 ±0.33
CaO	0.85 ±1.64	-0.01 ±0.02	/	0.56 ±0.06
FeO	0.23 ±0.11	0.17 ±0.07	10.80	0.18 ±0.09
MnO	0.00 ±0.04	-0.01 ±0.04	/	/
TiO <sub>2</sub>	0.03 ±0.04	-0.01 ±0.04	/	/
BaO	0.31 ±0.23	1.03 ±0.18	/	/
NiO	/	/	0.30	/
Total	101.50 ±0.90	101.15 ±0.98	99.80	101.11 ±2.12

EPMA analysis on sanidine 1 over 17 points, sanidine 2 over 15 points<sup>54</sup>, olivine San Carlos over 10 points<sup>56</sup> and on sanidine 1 after gas (air – 1<sub>wt.</sub>%Xe and Kr) doping at high *P-T* conditions (sample S1–13, see conditions in Extended Data Table 1). Abundances are given in <sub>wt.</sub>%. Errors reported are 2 standard errors.